Nuclear Engineering and Design 370 (2020) 110866

Contents lists available at ScienceDirect

Nuclear Engineering and Design

journal homepage: www.elsevier.com/locate/nucengdes

Towards model order reduction for fluid-thermal analysis

Kento Kaneko [a], Ping-Hsuan Tsai [b], Paul Fischer [a,b,*]

[a] Department of Mechanical Science and Engineering, University of Illinois at Urbana–Champaign, 1206 W. Green St. MC 244, Urbana, IL 61801, USA
[b] Department of Computer Science, University of Illinois at Urbana–Champaign, 201 North Goodwin Avenue MC 258, Urbana, IL 61801, USA

ARTICLE INFO

Keywords:
Reduced-order models
Model order reduction
Spectral element method
Boussinesq
Proper orthogonal decomposition (POD)
Parametric model order reduction

ABSTRACT

The authors develop basic components of a parametric model-order reduction (pMOR) procedure targeting high Rayleigh-number buoyancy-driven flows. The pMOR is based on Galerkin formulation of the governing Boussinesq equations using eigenfunction bases derived from proper orthogonal decomposition. The advantages of pMOR over parametric interpolation are demonstrated for quantities of interest (QOIs) with linear and nonlinear dependencies on the solution in low Rayleigh-number cases. Constraint-base and Leray-type regularizations are shown to offer significant advantages over the standard reduced-order Galerkin formulation in a variety of examples including 3D Rayleigh–Bénard flow at Rayleigh number 10^7 and turbulent flow in a half-pipe at Reynolds number 5300.

1. Introduction

High-performance computing and modern numerical algorithms have made high-fidelity fluid-thermal analysis tractable in geometries of ever increasing complexity. Despite continued advances in these areas, direct numerical (DNS), large-eddy (LES), and even unsteady Reynolds-averaged Navier–Stokes (uRANS) simulations of turbulent thermal transport remain too costly for routine analysis and design of thermal–hydraulic systems, where hundreds of cases must be considered. Reduced-order models (ROMs) offer a promising approach to leverage expensive high-fidelity simulations (referred to as full-order models or FOMs) by extracting from these detailed simulations low-dimensional dynamical systems that capture the principal features of the underlying flow fields (Merzari et al., 2009, 2011).

While FOMs for turbulent flows can require $\mathcal{N} = 10^7 - 10^{11}$ degrees-of-freedom, ROMs offer the potential of representing the flow dynamics governing the behavior of quantities of interest (QOIs) with only $N \approx 10^2$–10^3 basis functions. The amplitudes of these basis functions are typically evolved as a system of nonlinear ordinary differential equations (ODEs) or through other mechanisms, for example, based on machine learning (e.g., Lui and Wolf, 2019), or even through linearized models such as the recently-developed Green's function approach of Khodkar et al. (2019). For reasons of stability, Fick et al. (2018) replace ODE integration with a sequence of constrained-minimization problems that keep the ROM within observed bases of attraction.

The overall objective of *parametric model-order reduction* (pMOR) is to build ROMs from FOMs that are generated over a small set of *anchor* points $\mathcal{P}_\alpha = \{p_1^*, \ldots, p_m^*\}$ in the parameter space and to subsequently use the ROMs to inexpensively explore the parametric dependencies of the QOIs. To realize this goal, pMOR must address two problems: *(i)* the *reproduction problem*, in which a ROM accurately recovers QOIs for a turbulent flow simulation at a *particular* point in the parameter space (i.e., where the ROM and FOM are evaluated at the same p_j^*); and *(ii)* the *parametric problem*, in which the ROM provides estimates of QOIs at points $p \notin \mathcal{P}_\alpha$. To make the overall process efficient, the ROM should be equipped with error indicators to assess its fidelity at any given p, which allows one to optimally choose the anchor points p_j^*, thus minimizing the number of expensive FOMs required for effective parametric analysis (Fick et al., 2018). We typically choose the anchor points by evaluating the error indicator over a set of *training points*, $\mathcal{P}_\tau$ and selecting as the next element of $\mathcal{P}_\alpha$ the point that maximizes the error indicator in $\mathcal{P}_\tau$. In the present study, we do not consider error-indicated selection of $\mathcal{P}_\tau$; that topic is the focus of future work.

In this report, we present some basic steps towards realizing pMOR for buoyancy-driven turbulent flows at modest Rayleigh numbers. Initially, we consider the use of proper-orthogonal decomposition (POD) bases in a Galerkin formulation of the momentum and energy equations for relatively low Rayleigh-numbers. We show that pMOR is viable and significantly more accurate than parametric interpolation for both linear and nonlinear QOI examples. Second, we consider the closure problem for higher Rayleigh number cases, where ROMs typically suffer from

* Corresponding author.
E-mail address: fischerp@illinois.edu (P. Fischer).

https://doi.org/10.1016/j.nucengdes.2020.110866
Received 1 January 2020; Received in revised form 17 September 2020; Accepted 22 September 2020
Available online 1 November 2020

inadequate dissipation because of the lack of high-wavenumber functions in the POD approximation space. We consider two stabilization strategies. The first is a Leray-type regularization (Wells et al., 2017; Guermond et al., 2003), in which we mollify the nonlinear advection term by regularizing the *advecting field* (only). The second is based on the constrained-evolution approach of Fick et al. (2018), in which the snapshot data (introduced below) is reused to set limits on the basis coefficients in order to keep the dynamics of the system near the observed attractor. We demonstrate the relative success of these regularization approaches for two- and three-dimensional Rayleigh–Bénard convection in box-type geometries at Rayleigh numbers as high as 10^7. Finally, we demonstrate the effectiveness of constrained ROM for turbulent forced-convection in semi-circular pipe flow.

The rest of the paper is organized as follows. In Section 2, we briefly present the POD and the standard Galerkin ROM for the Boussinesq equations. In Section 3, we illustrate pMOR for the particular case of unsteady axisymmetric Rayleigh–Bénard convection with linear and nonlinear QOIs. In Section 4, we present Leray and constraint-based stabilization for higher Reynolds–Rayleigh-number applications. In Section 5, we demonstrate the importance of stabilization for several two- and three-dimensional examples. In Section 6, we demonstrate the potential of a mixed FOM/ROM application for cases featuring disparate hydro- and thermal-timescales. Finally, we draw conclusions and discuss future work in Section 7.

2. Galerkin-based ROM

Our point of departure is the Boussinesq approximation for buoyancy-driven flow,

$$\frac{\partial \mathbf{u}}{\partial t} + \Big(\mathbf{u}\cdot\nabla\Big)\mathbf{u} + \nabla p = \nu\nabla^2\mathbf{u} + \eta T\widehat{\mathbf{g}}, \nabla\cdot\mathbf{u} \;=\; 0, \tag{1}$$

$$\frac{\partial T}{\partial t} + \Big(\mathbf{u}\cdot\nabla\Big)T = \kappa\nabla^2 T, \tag{2}$$

subject to appropriate Dirichlet or Neumann boundary conditions for the velocity, $\mathbf{u}$, and temperature, T. Here p is the pressure, $\widehat{\mathbf{g}}$ is the unit vector in the (positive) vertical direction, and ν, η, and κ are problem parameters based on the nondimensionalization of the problem.

The ROM for the Boussinesq equations starts with a collection of K snapshots for velocity, $\mathbf{u}^k(\mathbf{x}) := \mathbf{u}(\mathbf{x}, t^k) - \mathbf{u}_b$ and for temperature, $T^k(\mathbf{x}) := T(\mathbf{x}, t^k) - T_b$ corresponding to numerical solutions of the full-order model (FOM) at well-separated timepoints, t^k, minus *base states*, $\mathbf{u}_b(\mathbf{x})$ and $T_b(\mathbf{x})$. The base states (typically time-averaged FOM solutions) satisfy any prescribed inhomogeneous boundary conditions, which are presently assumed to be time-independent.

The FOM is based on the spectral element method (SEM) in the open-source code, Nek5000, and uses the $\mathbb{P}_N - \mathbb{P}_N$ velocity–pressure coupling where the velocity and pressure are represented in the same polynomial bases.[1] For any $\mathbf{u}^k(\mathbf{x})$, we have a corresponding vector of basis coefficients $\underline{\mathbf{u}}^k = [\mathbf{u}_1^k \ldots \mathbf{u}_{\mathcal{N}}^k]^T$ such that $\mathbf{u}^k(\mathbf{x}) = \sum_{j=1}^{\mathcal{N}} \mathbf{u}_j^k \phi_j(\mathbf{x})$, with $\phi_j(\mathbf{x})$ the underlying spectral element basis functions spanning the FOM approximation space, $\mathbf{X}_0^{\mathcal{N}} \subset \mathcal{H}_0^1$. Because the SEM is nodal-based, each $\mathbf{u}_j^k$ represents the three velocity components at gridpoint $\mathbf{x}_j$ in the spectral element mesh at timepoint t^k. Similarly, the temperature is given by $T^k(\mathbf{x}) = \sum_{j=1}^{\mathcal{N}} T_j^k \phi_j(\mathbf{x}) \in X_0^{\mathcal{N}} \subset \mathscr{H}_0^1$. Here, $\mathscr{H}^1$ is the set of square-integrable functions on Ω whose gradient is also square-integrable and $X^{\mathcal{N}} \subset \mathscr{H}^1$ is the finite dimensional SEM approximation space spanned by $\{\phi_j(\mathbf{x})\}$. $\mathscr{H}_0^1$ is the set of functions in $\mathscr{H}^1$ that vanish wherever Dirichlet conditions associated with (2) are applied on the domain boundary $\partial\Omega$. Bold-face indicates that the space is spanned by vector-valued functions having d components ($d = 2$ or 3) and, in the case of $\mathbf{X}_0^{\mathcal{N}} \subset \mathcal{H}_0^1$, that the functions vanish where Dirichlet conditions are applied for (1).

[1] As described in Orszag et al. (1986), Tomboulides et al. (1989) and Tomboulides et al. (1997), the $\mathbb{P}_N - \mathbb{P}_N$ approach addresses the pressure boundary condition issue through temporal extrapolation of the velocity in curl-curl form to suppress growth of spurious divergence errors at the boundary.

2.1. POD bases

For the velocity, we collect the snapshots into the a matrix $\mathbf{U}_K = \Big[\underset{-}{\overset{1}{\mathbf{u}}} \ldots \underset{-}{\overset{K}{\mathbf{u}}}\Big]$. From these, one forms the Gramian, $\mathbf{U} \in \mathbb{R}^{K\times K}$, with $\mathbf{U}_{k,k'} := (\mathbf{u}^k, \mathbf{u}^{k'})_{L^2}$, where $(\mathbf{v}, \mathbf{u})_{L^2} := \int_\Omega \mathbf{v}\cdot\mathbf{u}\, dV$ is the L^2 inner product. We use the L^2 inner product throughout the paper. One could also consider the H^1 norm and H^1 semi-norm which have been considered in Iollo et al. (2000) and Fick et al. (2018). For the lower Reynolds number cases we have not found marked differences between the L^2 and H^1 inner products, so we use L^2 throughout the examples in the text. A careful comparison for the elevated Reynolds number cases will be the subject of future work.

Following standard POD methodology, the basis functions $\left\{\underset{-}{\overset{1}{\zeta}}, \ldots, \underset{-}{\overset{N}{\zeta}}\right\}$ for the ROM derive from the first N eigenmodes of $\mathbf{U}$,

$$\mathbf{U}\underset{-k}{z} = \lambda_k \underset{-k}{z}, \quad \underset{-k}{z} \in \mathbb{R}^K, \quad \lambda_1 \geqslant \cdots \geqslant \lambda_K \geqslant 0 \tag{3}$$

$$\underset{-n}{\zeta} := \mathbf{U}_K \underset{-n}{z}, \quad n = 1, \ldots, N < K. \tag{4}$$

The continuous functions in the SEM space corresponding to $\underset{-n}{\zeta}$ are $\zeta_n(\mathbf{x}) := \sum_{j=1}^{\mathcal{N}} \left(\underset{-n}{\zeta}\right)_j \phi_j(\mathbf{x})$.

We perform a similar procedure for temperature, generating $\mathbf{T}_K := \Big[\underset{-}{\overset{1}{T}} \ldots \underset{-}{\overset{K}{T}}\Big]$ and associated Gramian, $\mathbf{T}$, having entries $\mathbf{T}_{k,k'} := (T^k, T^{k'})_{L^2}$. We then solve the $K \times K$ eigenproblem,

$$\mathbf{T}\underset{-k}{\tau} = \lambda_k \underset{-k}{\tau}, \quad \underset{-k}{\tau} \in \mathbb{R}^K, \quad \lambda_1 \geqslant \cdots \geqslant \lambda_K \geqslant 0, \tag{5}$$

and define

$$\underset{-n}{\theta} := \mathbf{T}_K \underset{-n}{\tau}, \quad n = 1, \ldots, N < K. \tag{6}$$

The continuous functions in the SEM space corresponding to $\underset{-n}{\tau}$ are $\theta_n(\mathbf{x}) := \sum_{j=1}^{\mathcal{N}} \left(\underset{-n}{\theta}\right)_j \phi_j(\mathbf{x})$.

Remark 1. We note that, the POD construction provides a set of basis vectors $Z := \left\{\underset{-1}{\zeta}, \ldots, \underset{-N}{\zeta}\right\}$ that minimizes the average distance between Z and U_K in the chosen inner-product (here, $(\cdot,\cdot)_{L^2}$) for any rank-N subset of U_K. Thus, the motivation for POD is its approximation property, which uniformly distributes the error across the snapshot set. That property is not dependent on the subsequent choice of time-evolution of the ROM nor on any particular feature of the Navier–Stokes or Boussinesq equations. One could, however, consider other norms that might favor minimization of the errors in one or more QOIs, which is a topic for future consideration.

Remark 2. In the procedures that follow, we treat the velocity and temperature as independent state vectors. One could alternatively work

with snapshot sets that combine the velocity and temperature into a single vector and thus form the Gramian from $Q_K = \left[\underline{\underline{q}}^1 \ldots \underline{\underline{q}}^K\right]$, where $\underline{\underline{q}}^k := \left[\mathbf{u}^k\, T^k\right]$. This approach reduces the online evaluation cost of the ROM by a factor of two because one has one-half the number of variables to track. We anticipate a future study to compare cost-benefit trade-offs of these two approaches.

2.2. Galerkin formulation

With (optimal) basis sets in hand, the Galerkin formulation follows by inserting the reduced-basis expansions,

$$\tilde{\mathbf{u}}\left(x,t\right) = \sum_{n=0}^{N} \zeta_n\left(\mathbf{x}\right) u_n\left(t\right) \quad \in Z_b \tag{7}$$

$$\tilde{T}\left(x,t\right) = \sum_{n=0}^{N} \theta_n\left(\mathbf{x}\right) T_n\left(t\right) \quad \in \Theta_b, \tag{8}$$

into the weak form of (1)–(2). In order to set the boundary conditions, we have augmented the trial (approximation) spaces Z_b and Θ_b with the base states, $\zeta_0 := \mathbf{u}_b$ and $\theta_0 := T_b$. The coefficients for these terms are prescribed: $u_0 \equiv T_0 \equiv 1$. The corresponding test spaces, $Z_0 := \{\zeta_i\}_{i=1}^N$ and $\Theta_0 := \{\theta_i\}_{i=1}^N$, satisfy homogeneous boundary conditions, as is standard for Galerkin formulations.In weak form, the problem can be stated as *Find* $\tilde{\mathbf{u}} \in Z_b, \tilde{T} \in \Theta_b$*, such that, for all* $\mathbf{v} \in Z_0, S \in \Theta_0$*,*

$$\int_\Omega \mathbf{v}\cdot\frac{d\tilde{\mathbf{u}}}{dt}\,dV + \nu\int_\Omega \nabla\mathbf{v} : \nabla\tilde{\mathbf{u}}\,dV = -\int_\Omega \mathbf{v}\cdot(\tilde{\mathbf{u}}\cdot\nabla)\tilde{\mathbf{u}}\,dV + \eta\int_\Omega \mathbf{v}\cdot\left(\tilde{T}\hat{\mathbf{g}}\right)dV, \tag{9}$$

$$\int_\Omega S\frac{d\tilde{T}}{dt}\,dV + \kappa\int_\Omega \nabla S\cdot\nabla\tilde{T}\,dV = -\int_\Omega S(\tilde{\mathbf{u}}\cdot\nabla)\tilde{T}\,dV + \kappa\int_{\partial\Omega_f} S\nabla\tilde{T}\cdot\hat{\mathbf{n}}\,dA. \tag{10}$$

We remark that the presence of the surface integral in (10) admits the possibility of an inhomogeneous surface flux $q_s := \kappa\nabla\tilde{T}\cdot\hat{\mathbf{n}}$ on some part of the domain boundary $\partial\Omega_f \subset \partial\Omega$. If ζ_0 and θ_0 satisfy the prescribed Dirichlet conditions, then $\tilde{\mathbf{u}}$ and $\tilde{T}$ will satisfy these conditions as well. Note that the pressure term vanishes from (9) as a result of integration-by-parts because the test functions are weakly divergence-free and they are all homogeneous on the boundary. The continuity equation of the Navier–Stokes equations is also removed since Z_b consists solely of weakly divergence-free basis functions. For temporal discretization of (9)–(10), we use a semi-implicit scheme with kth-order backward differencing (BDFk) for the time derivative, implicit treatment of the negative-definite dissipation terms, and kth-order extrapolation (EXTk) of the advection and buoyancy terms. We typically use $k = 3$, to ensure that the imaginary eigenvalues associated with skew-symmetric advection operator are within the stability region of the BDFk/EXTk time-stepper, as discussed in Fischer et al. (2017). When fully discretized in space and time, we get the following systems for the ROM basis coefficients $\underline{\underline{u}}^n$ and $\underline{\underline{T}}^n$ at timepoint t^n,

$$\left(\frac{\beta_0}{\Delta t}B_u + \nu A_u\right)\underline{\underline{u}}^n = -\sum_{i=1}^{k}\alpha_i\left[C_u\left(\underline{\underline{u}}\right)\underline{\underline{u}} - \eta B_{uT}\underline{\underline{T}}\right]^{n-i} - B_u\sum_{i=1}^{k}\frac{\beta_i}{\Delta t}\underline{\underline{u}}^{n-i} - \nu\underline{\underline{a}}_{u,0}, \tag{11}$$

$$\left(\frac{\beta_0}{\Delta t}B_T + \kappa A_T\right)\underline{\underline{T}}^n = -\sum_{i=1}^{k}\alpha_i\left[C_T\left(\underline{\underline{u}}\right)\underline{\underline{T}}\right]^{n-i} - B_T\sum_{i=1}^{k}\frac{\beta_i}{\Delta t}\underline{\underline{T}}^{n-i} - \kappa\underline{\underline{a}}_{T,0} + \underline{\underline{q}}_s. \tag{12}$$

Here, $\underline{\underline{u}}$ and $\underline{\underline{T}}$ are the augmented basis vectors that include the base states for $\underline{\underline{u}}$ and $\underline{\underline{T}}$; α_i and β_i are the respective BDFk/EXTk coefficients (e.g., for $k = 2$, $\alpha_1 = 2, \alpha_2 = -1, \beta_0 = \frac{3}{2}, \beta_1 = -\frac{4}{2}$, and $\beta_2 = \frac{1}{2}$). A,B, and C represent the respective stiffness, mass, and advection operators, with entries

$$A_{u,ij} = \int_\Omega \nabla\boldsymbol{\zeta}_i : \nabla\boldsymbol{\zeta}_j\,dV \tag{13}$$

$$B_{u,ij} = \int_\Omega \boldsymbol{\zeta}_i\cdot\boldsymbol{\zeta}_j\,dV \tag{14}$$

$$C_{u,ikj} = \int_\Omega \boldsymbol{\zeta}_i\cdot\left(\boldsymbol{\zeta}_k\cdot\nabla\right)\boldsymbol{\zeta}_j\,dV \tag{15}$$

$$A_{T,ij} = \int_\Omega \nabla\theta_i\cdot\nabla\theta_j\,dV \tag{16}$$

$$B_{T,ij} = \int_\Omega \theta_i\theta_j\,dV \tag{17}$$

$$C_{T,ikj} = \int_\Omega \theta_i\cdot\left(\boldsymbol{\zeta}_k\cdot\nabla\right)\theta_j\,dV. \tag{18}$$

$$B_{uT,ij} = \int_\Omega \boldsymbol{\zeta}_i\cdot\hat{\mathbf{g}}\theta_j\,dV \tag{19}$$

$$\underline{\underline{q}}_{s,i} = \int_{\partial\Omega_f}\theta_i\,q_s\,dA \tag{20}$$

Remark 3. The computational cost of time-advancing (11) and (12) is dominated by the application of the rank-3 advection tensors, C_u and C_T, which requires $O(N^3)$ operations and memory references on each step. The remainder of the terms are $O(N^2)$ or less. Unfortunately, $O(N^3)$ is a very steep cost and prohibits practical consideration of, say, $N > 500$. While not considered here, strategies to mitigate this cost are of paramount concern.

We have applied the Galerkin-ROM formulation (11)–(12) for several cases, including the basic test problem of two-dimensional flow past a cylinder at Reynolds number $Re_D = 100$, for which $N \approx 20$ provides a sufficient number of modes for accurate reproduction of the flow field and the lift history to four significant digits. As stated earlier, however, our objective is not reconstruction of the flow field. Rather, we aim to predict QOIs at parameter points p that are not in the set $\mathscr{P}_{\text{anchor}}$ from which we draw our approximating bases. In the next section, we illustrate use of the Galerkin ROM for both the reproduction and pMOR problems in the case of a axisymmetric Rayleigh–Bénard convection.

3. Parametric model order reduction

Given that the parameters and QOIs for thermal-fluids applications are highly case specific, we introduce pMOR in this section in the context of a particular model problem. Specifically, we consider the temporal-behavior of the Nusselt number in axisymmetric Rayleigh–Bénard convection, which was studied by Barkley and Tuckerman (1989).

3.1. Axisymmetric Rayleigh–Bénard problem

The spatial domain is a low aspect-ratio cylinder and, following (Barkley and Tuckerman, 1989), the problem is cast in cylindrical coordinates with $[r,z] \in [0,R]\times[0,H]$ ($R = 5$, $H = 1$), so the flow is effectively two-dimensional. For velocity, we have $\mathbf{u} = 0$ on the upper, lower, and side walls. For temperature, we have $T = 1 - z$ on those surfaces. At $r = 0$, the radial component of the velocity is zero while the vertical component and temperature have homogeneous Neumann conditions.

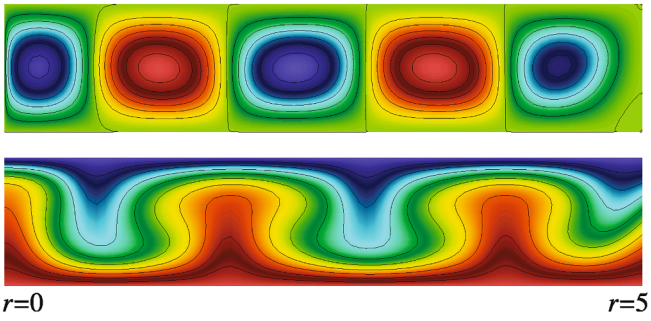

Fig. 1. Stream-function (top) and temperature (bottom) from an FOM snapshot for axisymmetric Rayleigh–Bénard problem with $\epsilon = 2.60$.

The problem is nondimensionalized with a viscous timescale, resulting in parameters $\nu = \mathrm{Pr}, \eta = \mathrm{Ra}\,\mathrm{Pr}$, and $\kappa = 1$, where Ra is the Rayleigh number and Pr is the Prandtl number.

Above a critical Rayleigh number, Ra_c, this flow exhibits an unsteady phenomenon in which vortex rings formed at the outer edge of the cylinder push the interior vortex rings inwards and squeeze out the one at the center. The orientation of the vortices thus periodically flips, with the net effect being that we see a traveling wave of inward moving rings. For $Ra > Ra_c$, the period of this phenomenon increases as $Ra \longrightarrow Ra_c$. Our goal is to reproduce the FOM results as a function of $\epsilon = (\mathrm{Ra} - \mathrm{Ra}_c)/\mathrm{Ra}_c$ over a range of Rayleigh numbers by performing FOM simulations at only one or two Rayleigh numbers. We take as our parametric domain $\epsilon \in [1.60, 2.60]$ and as our QOI the transition period, indicated by fluctuations in the Nusselt number. By performing this study, we wish to establish the feasibility of pMOR for thermally-driven flows. Our FOM is based on the axisymmetric formulation in Nek5000 using a 4×1 array ($r \times h$) of 15th-order spectral elements. The FOM is based on 3rd-order semi-implicit timestepping with timestep size $\Delta t = 4 \times 10^{-4}$. The physical parameters are Ra_c=1734, $Pr = 10$, domain radius $R = 5$, and height $H = 1$. From the FOM, the Nusselt number period is 41.200 for $\epsilon = 1.60$ and 15.984 for $\epsilon = 2.60$, in accord with the results in Barkley and Tuckerman (1989). One snapshot from the problem for $\epsilon = 2.60$ is shown in Fig. 1.

3.2. pMOR setup

Our parametric model-order reduction approach follows the *p-greedy* algorithm described in Fick et al. (2018) in which we combine basis sets from two points in the ϵ-parameter space to form one large approximation space. We first start by running FOM simulations using $\epsilon = 1.60$ and $\epsilon = 2.60$ to obtain two sets of snapshots, taken over 200 Time-Units and spaced equally by 0.1 Time-Units. Then, for each set, we form the velocity Gramian matrix by taking the inner product of the velocity snapshots and form the temperature Gramian matrix by taking the inner product of the temperature snapshots. For each set, using these Gramian matrices, we can obtain 20 dominant velocity modes and 20 dominant temperature modes. We use a total of 40 combined velocity modes and 40 combined temperature modes from this procedure as the basis functions for the Galerkin projection. Once the basis functions for the velocity and temperature are generated, the various operators in the systems can be formed as shown in (13)–(20). (Note that the integrands must be modified to account for the axisymmetric coordinates. This modification is straightforward in Nek5000 because the operator interfaces are independent of the number of space dimensions or type of domain.) Although the physics is fully coupled, the ROM time-stepping is performed separately for the velocity and temperature fields by the use of extrapolation for the advection terms. Thus, the 3rd rank tensors C_T and C_U are created with 40 basis functions for each field; resulting in

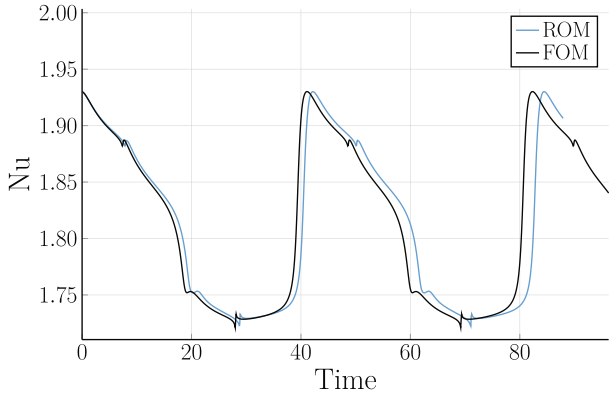

Fig. 2. Nusselt number for $\epsilon = 1.60$.

40^3 entries[2] in each of the advection tensors. In short, although we are using 80 total velocity and temperature basis functions, the total cost of evaluating the convection for both equations is 2×40^3 multiplication operations, instead of 80^3 multiplications.With this setup, we adjust the parameters in (11)–(12) to run the ROM for $\epsilon \in \{1.6, 1.65, \ldots, 2.6\}$. The endpoint data, $\epsilon = 1.6$ and 2.6, are used to generate the parametric model while the interior points are used for verification of the pMOR procedure. Presently, we use the same timestep size for the ROM as for the FOM, but this choice is not strictly necessary. For each ϵ, we obtain Nusselt number vs. time behavior after first having let the flow settle to a steady-periodic state for 100 time units. We extract the period from the subsequent 100-unit time interval.

3.3. Computation of the Nusselt number

The Nusselt number for this problem is defined as:

$$\mathrm{Nu} = \frac{2H}{R^2 \Delta T} \int_0^R T_z\left(r, 0, t\right) r\, dr, \tag{21}$$

where $\Delta T = 1$ is the temperature differential between the upper and lower surfaces. Calculation of Nu by reconstructing the FOM temperature field from the basis coefficients will result in a heavy computational cost of $O(\mathcal{N} \times N)$ where $\mathcal{N}$ is the total number of degrees of freedom for the FOM.

Fortunately, because Nu is a linear functional in T, it can be calculated indirectly by computing the contribution from each basis function to the sum in the offline (FOM) phase without reconstruction of the solution at each timestep in the online (ROM) phase. Specifically,

$$\mathrm{Nu}\left(\mathrm{t}\right) = \frac{2H}{R^2 \Delta T} \int_0^R \sum_{i=0}^{N} T_i\left(t\right) \theta_{i,z}\left(r, 0\right) r\, dr \tag{22}$$

$$= \frac{2H}{R^2 \Delta T} \sum_{i=0}^{N} T_i\left(t\right) \int_0^R \theta_{i,z}\left(r, 0\right) r\, dr \tag{23}$$

$$= \frac{2H}{R^2 \Delta T} \sum_{i=0}^{N} T_i\left(t\right) I_i \tag{24}$$

We calculate the I_i in the offline phase so we can determine the Nusselt number in the online phase without any knowledge of the FOM (i.e., SEM) bases. Thus, the computational cost of evaluating the Nusselt number at each timestep in the ROM is only $O(N)$.

To calculate the period of the Nusselt number, we subtract the mean

[2] The full C_T contains $40 \times 40 \times 41$ elements, with the extra elements arising from the inhomogeneous boundary term.

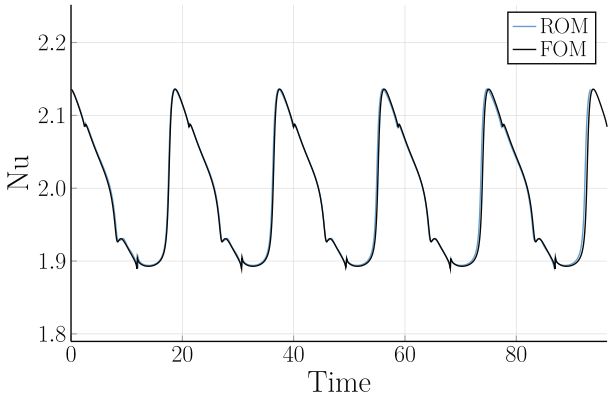

Fig. 3. Nusselt number for $\epsilon = 2.35$.

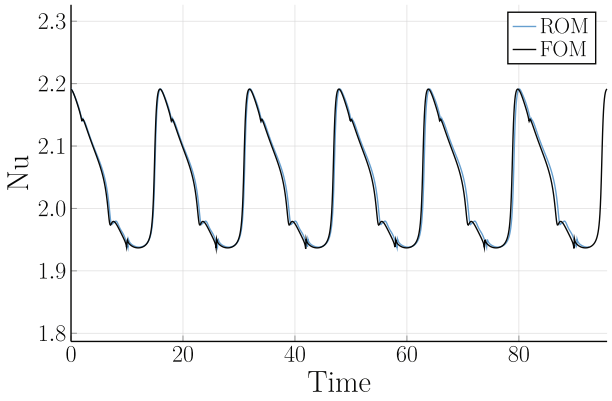

Fig. 4. Nusselt number for $\epsilon = 2.60$.

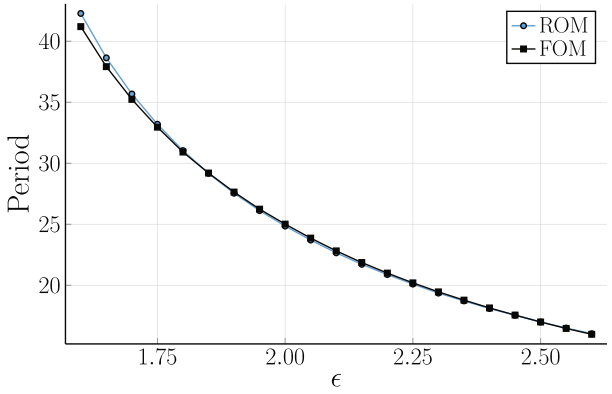

Fig. 5. Period comparison of FOM and *p*-greedy ROM using two anchor points at $\epsilon = 1.60$ and 2.60.

value from the data and measure the average time between successive downward zero-crossings over the final 100 time units. We note that the period is *not* a linear functional of the solution but is nonetheless accessible via an accurate ROM.

3.4. pMOR results

Figs. 2–4 show the Nusselt number histories for the FOMs and ROMs at $\epsilon = 1.60, 2.35$, and 2.60. The 1.60 and 2.60 cases correspond to anchor points in the pMOR study—the ROM bases derive directly from FOMs at these parameter values. The 2.35 case derives from projection onto the 40×2 basis vectors and is thus truly the result of pMOR-driven analysis. We remark that, even at the anchor points (e.g., $\epsilon = 1.60$), the histories are not perfect. This discrepancy arises because the time-dependent ROM is not a perfect reconstruction of the FOM.

In Fig. 5, we see good agreement between the FOM data and the ROM data. The largest error is found at $\epsilon = 1.60$, with a difference of 1.08 (i.e., ≈2.6% relative error). Thus, for this problem, instead of running a FOM simulation for all 21 points, we can obtain fairly accurate results by running 2 FOM simulations and running pMOR on all the points. Furthermore, if a period value for an additional ϵ within the range is desired, the ROM, without any modification, can obtain that value fairly accurately.

We note that the potential value of the pMOR procedure is clearly evident in this example. If one only had knowledge of the period at the points $\epsilon = 1.6$ and 2.6, there would be little recourse but to estimate the periods at interior points through linear interpolation, which leads to ≈20% overestimate of the period at $\epsilon \approx 2$. The low-rank dynamical system of the ROM does a remarkably good job of improving upon this estimate.

4. Stabilization

A significant issue with the standard Galerkin-based ROM at higher Reynolds numbers is that (11)–(12) can deviate substantially from the projection of the modes onto the FOM due to the presence of potentially spurious attractors. This unstable behavior is an artifact of modal truncation (often manifest as energy pile-up in the high wavenumber modal coefficients) and relates to the well-known closure problem in LES and other turbulence-modeling scenarios (Fick et al., 2018; Rempfer, 2000). The smoothness of the approximating modes $\{\zeta_n\}$ prevents generation of adequate dissipation (through $Re^{-1}(\zeta_j, \zeta_j)_A$) unless the corresponding coefficients have large amplitude. One can potentially resolve this issue by increasing N to the point where the reduced bases include modes capable of dissipating the energy. For turbulent flows, however, the number of required modes can be quite high, particularly in light of the $O(N^3)$ costs associated with the advection operators C_u and C_T. Hence, for engineering applications, some sort of closure model is typically required to dissipate energy or otherwise stabilize the ROM.Here, we consider two stabilization approaches. The first is a relatively simple Leray-type regularization introduced in the ROM context by Wells et al. (2017). The second is the constraint-based ROM of Fick and co-workers (Fick et al., 2018). While our primary focus is on the latter, the Leray-based approach is both easy to implement and elegant. We feel compelled to consider it because of the insight it lends to POD-based reduced-order modeling.

4.1. Leray regularization

For the Navier–Stokes equations, Leray regularization amounts to filtering the *advecting* field, such that the momentum equation reads

$$\frac{\partial \mathbf{u}}{\partial t} + \left(\bar{\mathbf{u}}\cdot\nabla\right)\mathbf{u} + \nabla p = \nu\nabla^2\mathbf{u} + \eta T\hat{\mathbf{g}}, \tag{25}$$

where $\bar{\mathbf{u}} = F(\mathbf{u})$ is the result of some sort of smoothing or regularization of the current velocity field. As noted by Guermond et al., even just a small amount of regularization suffices to make gains in proving existence and uniqueness of the solution in the continuous case, a task that remains insurmountable for the full Navier–Stokes equations. Thus, Leray regularization is of interest both from a numerical (and physical) stabilization viewpoint and from a theoretical perspective.

Guermond et al. (2003) discuss a Helmholtz filter of the form

$$\bar{\mathbf{u}} = \left(1 - \delta^2\nabla^2\right)^{-1}\mathbf{u}, \tag{26}$$

which is a 2nd-order filter that suppresses modes of wavenumber $k > 1/\delta$ at a rate $\tilde{O}(k^2)$ and which can be implemented in general geometries (e.g., Mullen, 1999).

For Fourier-based discretizations, filtering is particularly simple as one can simply scale the wavenumber coefficients, $\widehat{\overline{\mathbf{u}}}_k = \sigma_k \widehat{\mathbf{u}}_k$, where $\sigma_k \longrightarrow 1$ as $k \longrightarrow 0$ and $\sigma_k \longrightarrow 0$ as $k \longrightarrow \infty$.

For the Galerkin-based ROM, the modification equivalent to (25) would be to replace $\widetilde{\mathbf{u}}$ by $\overline{\mathbf{u}}$ in the energy Eq. (10) and to similarly replace the advector in the momentum Eq. (9) to yield

$$\int_\Omega \mathbf{v}\cdot\frac{d\widetilde{\mathbf{u}}}{dt}\,dV + \nu\int_\Omega \nabla\mathbf{v} : \nabla\widetilde{\mathbf{u}}\,dV = -\int_\Omega \mathbf{v}\cdot(\overline{\mathbf{u}}\cdot\nabla)\widetilde{\mathbf{u}}\,dV + \eta\int_\Omega \mathbf{v}\cdot\left(\widetilde{T}\widehat{\mathbf{g}}\right)dV. \quad (27)$$

Wells et al. (2017) consider several possible filters to map $\widetilde{\mathbf{u}}$ to $\overline{\mathbf{u}}$. The simplest one, suggested by one of the authors, is to treat the POD modes as one would do with Fourier bases (personal communication, 2019). That is, one can simply damp out the amplitudes of the higher modes when constructing $\overline{\mathbf{u}}$ in (27). In the following Leray-ROM examples, we do precisely that. We use a sharp cut-off filter in which we set a few of the highest-numbered basis coefficients to zero when constructing the advector, $\overline{\mathbf{u}}$. Notice that this approach, while blunt, also has the advantage of reducing the leading-order $O(N^3)$ cost of evaluating the advection terms. As seen in the examples at the end of this section, simple Leray regularization is remarkably effective and merits further development. One improvement is to use the differential filter (26), which is readily implemented in the POD bases by using (13) and (14). This approach was shown in Wells et al. (2017) to be superior to simple modal damping for the example of three-dimensional flow past a cylinder at $Re = 1000$.

4.2. Constrained optimization

As an alternative to explicitly adding dissipation or other closure terms, Fick et al. (2018) suggest a novel strategy of replacing the equality (11) with a constrained minimization problem at each timestep that would keep the dynamical system near the attractors observed in the snapshot set. We briefly describe that approach here.The standard Galerkin formulation (11) requires the following system to be solved for the velocity at each timestep,

$$H_u \underline{\overset{n}{u}} = \underline{\overset{n}{g}}, \quad (28)$$

where the Helmholtz matrix,

$$H_u := \frac{\beta_0}{\Delta t}B_u + \nu A_u. \quad (29)$$

is based on (13)–(14) and the right-hand side is

$$\underline{\overset{n}{g}} = -\sum_{i=1}^{k}\left[\frac{\beta_i}{\Delta t}B_u \underline{\overset{n-i}{u}} + \alpha_i\left(C_u\left(\underline{\overline{u}}\right)\underline{\overline{u}} - \eta B_{uT}\underline{\overline{T}}\right)^{n-i}\right] - \nu\underline{a}_0. \quad (30)$$

We note that H_u is a symmetric positive definite matrix.

The idea behind the constrained formulation is to use information from the snapshot set to establish *a priori* bounds on the basis coefficients $\underline{\overset{n}{u}}$ by replacing (28) with the constrained optimization problem,

$$\underline{\overset{n}{u}} = \arg\min_{\underline{u}\in\mathscr{R}^N} \frac{1}{2}\|H_u\underline{u} - \underline{\overset{n}{g}}\|^2_{H^{-1}}, \text{ s.t. } m_j \leqslant u_j^n \leqslant M_j. \quad (31)$$

where the constraints on the basis coefficients $u_j^n, j = 1,\ldots,N$ are derived from the observation snapshot set, $\mathbf{U}_K$. Let Γ be the $N \times K$ matrix with entries $\gamma_{jk} := (\zeta_j, \mathbf{u}^k)_A$, which correspond to the modal amplitudes for each snapshot $\mathbf{u}^k$. For each basis function ζ_j, we set $m_j = \min_k \gamma_{jk}$ and $M_j = \max_k \gamma_{jk}$ such that the ROM *evolution* of the basis coefficients is constrained by the observed values from the snapshot set. (In practice, each window $[m_j, M_j]$ is increased a few percent.) *Thus, this scheme reuses the snapshot information to adjust the behavior of the dynamical system.*

To solve the inequality-constrained optimization problem, we modify the original objective function by adding barrier functions to convert (31) into a sequence of unconstrained problems with small parameter μ_k,

$$\phi\left(\underline{u}\right) := f\left(\underline{u}\right) - \mu_k\sum_{i=1}^{N}\left(\frac{1}{m_i - u_i} + \frac{1}{u_i - M_i}\right), \quad (32)$$

where

$$f\left(\underline{u}\right) = \frac{1}{2}\underline{u}^T H_u \underline{u} - \underline{u}^T\underline{g} + \frac{1}{2}\underline{g}^T H_u^{-1}\underline{g}. \quad (33)$$

For successively smaller values of μ_k we solve (32) with the Broyden–Fletcher–Goldfarb–Shanno (BFGS) method using the preceding solution as a starting point. By letting $\mu_k \to 0$ as $k \to \infty$, the barrier problems (32) recover (31).

We remark that each iteration of BFGS requires the solution of an approximate Hessian, H_l associated with the augmented objective function ϕ. Starting the procedure with $H_1 = H$ as the initial Hessian requires solving systems in H for each iteration $l = 1, 2, \ldots$, plus application of a rank-2 Sherwin–Morrison type correction to effect the inverse of the updated Hessian (Nocedal, 1980). Note that the cost for solving the Hessian is $\mathscr{O}(N^2)$ per iteration. We introduce a new approach that reduces the cost per iteration from $\mathscr{O}(N^2)$ to $\mathscr{O}(N)$ and provides a significant savings in the constraint-based ROM. The idea is to recast the unknowns into an H-orthogonal basis such that the initial Hessian is diagonal. Specifically, we consider the similarity transformation $H = W\Lambda W^T$ with W^T an orthonormal rotation matrix. With substitutions $\underline{u} = W\underline{\widehat{u}}$ and $\underline{g} = W\underline{\widehat{g}}$, the original objective function is transformed to

$$\widehat{f}\left(\underline{\widehat{u}}\right) = \frac{1}{2}\underline{\widehat{u}}^T\Lambda\underline{\widehat{u}} - \underline{\widehat{u}}^T\underline{\widehat{g}} + \frac{1}{2}\underline{\widehat{g}}^T\Lambda^{-1}\underline{\widehat{g}}, \quad (34)$$

where Λ is a diagonal matrix. Since the (one-time) transformation cost for a particular H_u is $O(N^3)$ and the transformation cost per time-step is $O(N^2)$, we do not increase the complexity of the problem. Also, we do not need to recompute the QOI factors since they can be computed in the original space. In other words, no additional offline-mode computation is required for each ROM run.

To keep the simple (decoupled) form of the limits (32), we re-evaluate the limits in this transformed space, which can be done if we preserve the matrix Γ, computed in the off-line mode. Since Γ has only $NK \ll \mathscr{N}$ entries it can be used in the online mode and typically needs to be referenced only at the beginning of the ROM advancement when the parameters $(\beta_0, \Delta t, \nu)$ are set. The original limits were $m_j = \min_k \gamma_{jk}$ and $M_j = \max_k \gamma_{jk}$, for $j = 1,\ldots,N$. In this modified setting, the new limits are $m_j' = \min_k \gamma_{jk}'$ and $M_j' = \max_k \gamma_{jk}'$, where γ_{jk}' are the entries of

$$\Gamma' := W^T\Gamma.$$

Because W is orthonormal, these limits correspond to an N-dimensional bounding-box that contains the projected amplitudes in a rotated frame of reference. This new frame of reference simply reflects a different choice of norm, here the H-norm, which is a combination of the L^2 and energy inner-products and is therefore just as physically justifiable as either of these norms on their own. In either framework, the solution recovers to that of (28) if the constraints are inactive.

4.3. Costs of stabilization

Examples of the online costs of the methods we've considered so far are presented in Table 1. The case under consideration is the lid-driven cavity at $Re_L = 30{,}000$, which is described in the next section. The ROM integration time is 1500 convective time units. As expected, the

Table 1
Solve time comparisons for lid-driven cavity example of Fig. 6 integrated over 1500 convective time units, using $N = 40$ for the ROMs.

	Solve Time (s)
Galerkin ROM	0.242
Leray ROM	0.244
Constrained ROM w/o Decoupling	156.4
Constrained ROM w/ Decoupling	68.57
SEM Full-Order Model	1112

Galerkin- and Leray-ROM cases are comparable in time. The constrained optimization solvers are significantly slower, but still much faster than the SEM-based FOM, which was run with 256 spectral elements of order $p = 7$. We remark that there is room for significant improvement in the optimization solver as we did not use highly-tuned optimization packages that would minimize the number of iterations required for the interior-point methods that we employed to solve (31).

5. Results for stabilized methods

In the following, we present results for several examples in which we compare stabilized and unstabilized methods. We reiterate that our Leray-ROM examples do not represent an exhaustive study of this approach, but are included merely to show the potential of this remarkably simple strategy, as put forth in Wells et al. (2017).

5.1. Lid-driven cavity

Here, we apply these concepts to two model problems. First, we reproduce work done by Fick et al. (2018) with the Lid-Driven Cavity Problem. Then we add the advection–diffusion equation to the NSE to show the effect of the constrained optimization on a relevant QOI which is the Nusselt number. We also apply Leray regularization to compare the effectiveness of the two stabilization techniques.

Following Fick et al. (2018), we consider the unsteady lid-driven cavity problem using parameter $\nu = \frac{1}{\mathrm{Re}}$ and $\eta = 0$ subject to steady boundary conditions.

$$\begin{cases} \mathbf{u} = \mathbf{u}_b & \text{on } \Gamma_{top} \times \mathscr{R}_+, \\ \mathbf{u} = 0 & \text{on } \partial\Omega \backslash \Gamma_{top} \times \mathscr{R}_+, \\ \mathbf{u} = 0 & \text{on } \Omega \times \{0\}, \end{cases} \tag{35}$$

where $\mathbf{u} : \Omega \times \mathscr{R}_+ \to \mathscr{R}^2$ is a two-dimensional vector field, $\Omega = [-1, 1]^2$, $\Gamma_{top} = \{\mathbf{x} \in \overline{\Omega} : x_2 = 1\}$, and the Dirichlet datum is given by

$$\mathbf{u}_b\left(\mathbf{x}\right) = \begin{bmatrix} \left(1 - x_1^2\right)^2 \\ 0 \end{bmatrix}. \tag{36}$$

The FOM results were produced using Nek5000 (Fischer et al., 2008)

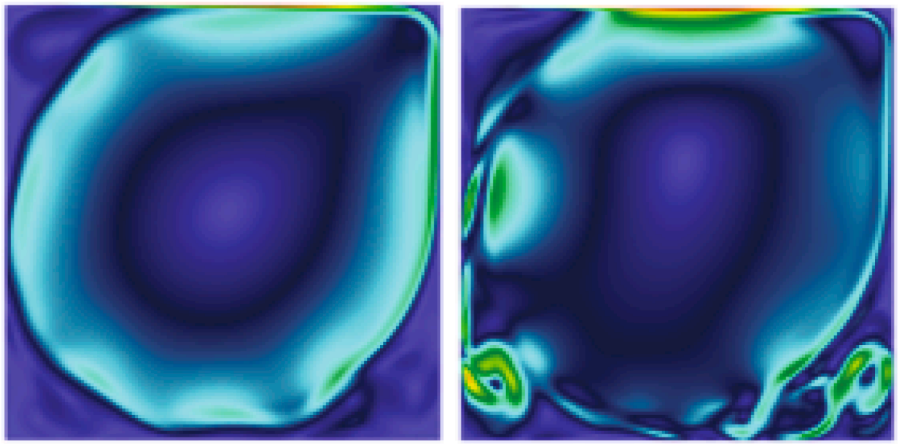

(a) FOM (b) Galerkin ROM

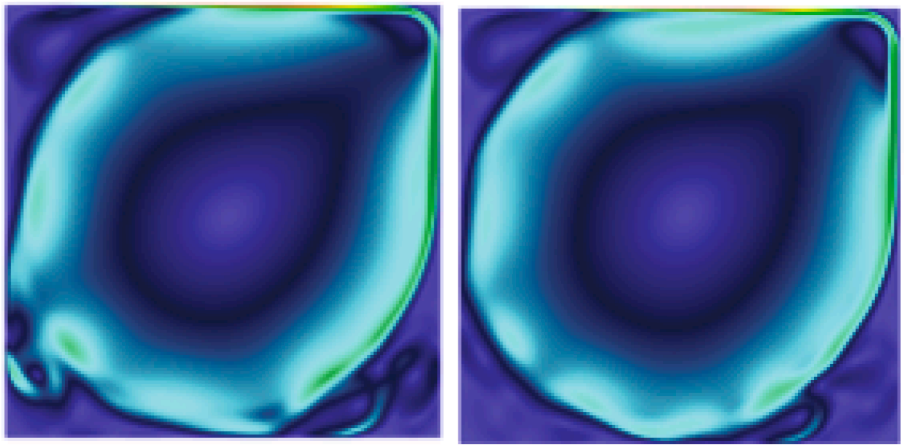

(c) Leray ROM (d) Constrained ROM

Fig. 6. Velocity magnitude comparison at $t = 1740$ between the FOM, and the Galerkin, Leray, and constrained ROMs with $N = 20$.

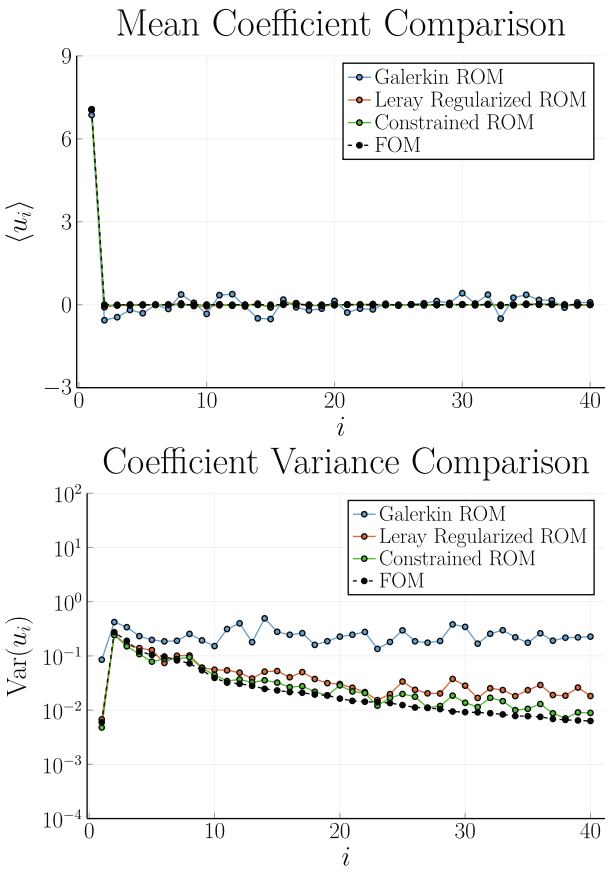

Fig. 7. Behavior of the sample mean and variance of the coefficients $\{u_n^j\}_j$ for the lid-driven cavity with $N = 40$.

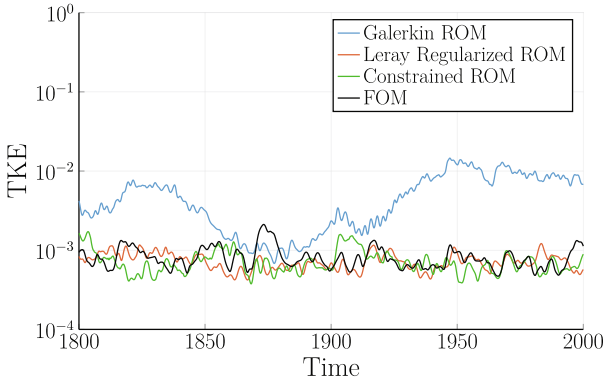

Fig. 8. TKE behavior comparison for FOM, Galerkin ROM, Leray ROM and constrained ROM with $N = 40$.

with 256 spectral elements of order $N = 7$ at $\mathrm{Re} = 30,000$. In order to generate the ROM solution, we collect 500 snapshots at the sampling times $\{t_s^k = 500 + \Delta t_s k\}_{k=1}^{K}$ with $\Delta t_s = 1$ and $K = 500$, where the data are taken from the statistically steady state solution. For the lid-driven cavity problem, we also apply the Leray regularization for the ROM. The velocity magnitude at time $t = 1740$ is shown in Fig. 6 for the FOM, and for the Galerkin, Leray, and constrained ROMs, each using $N = 20$.

Fig. 7 shows the sample mean and variance for the FOM, Galerkin ROM, Leray ROM, and constrained ROM. We observe that the results for the Leray regularization and the constrained ROM are superior to those of the Galerkin ROM.

Fig. 8 shows the estimated TKE,

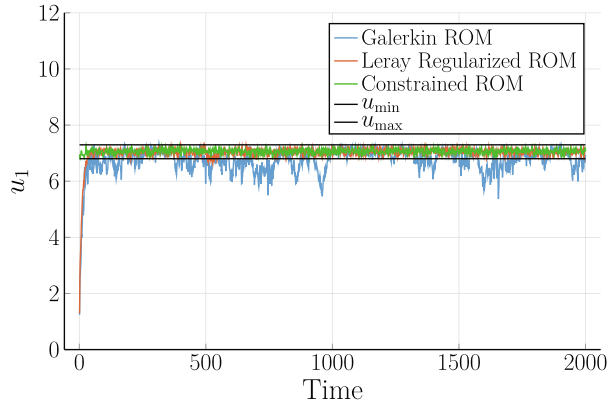

Fig. 9. Comparison of the first mode behavior for various stabilization techniques with $N = 40$.

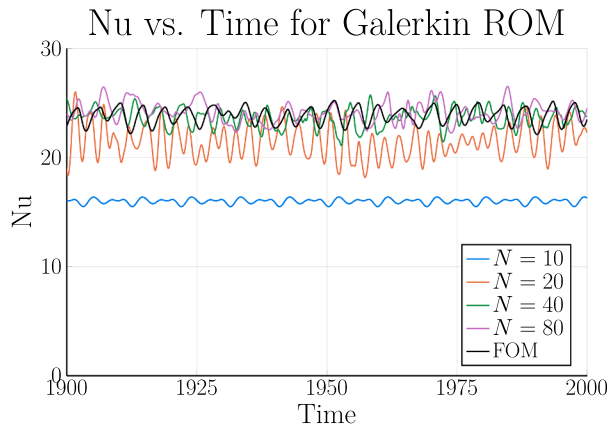

Fig. 10. Heated lid-driven cavity Nusselt number vs. time for Galerkin ROM with various N.

$$\mathrm{TKE}\left(t\right) = \frac{1}{2}\int_{\Omega} \|\mathbf{u}\left(x,t\right) - \left\langle \mathbf{u} \right\rangle\left(x\right)\|_2^2, \tag{37}$$

where $\|\cdot\|_2$ is the Euclidean norm. The Galerkin, Leray, and constrained ROMs using $N = 40$ are compared with the FOM. For the Leray regularization, the last 50% of the modes are set to zero. Note that the percentage of modes to be filtered is not known beforehand. For this problem, we have tried filtering out 10%, 20%, 30%, 40% and 50%, and found that 50% produced the most accurate results. The question of optimal filter choice depends on the number of POD modes and on the problem and will be a topic of future study.

To further demonstrate the effects of stabilization, we plot the coefficient behavior versus time. Fig. 9 clearly shows that, without regularization, the coefficient for the first POD basis function ventures out of the range observed in the data. Other spurious phenomena include effects such as false stable steady flows.

As thermal transport is one of our principal motivators, we consider an energy transport problem using parameter $\kappa = \frac{1}{\mathrm{Re}}$ with the solution to the lid-driven cavity problem as the advecting field. The thermal boundary conditions are:

$$\begin{cases} T(x,-1,t) = 0, \\ T(x,1,t) = 1, \\ T(x,-1,t) = T(x,1,t) = 1. \end{cases} \tag{38}$$

The QOI is the Nusselt number, which is the mean temperature gradient

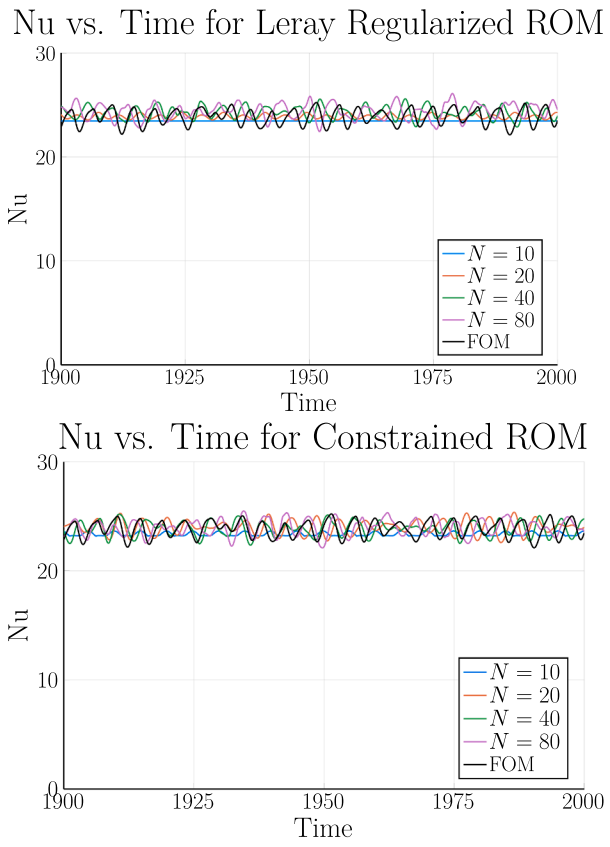

Fig. 11. Heated lid-driven cavity Nusselt number vs. time for ROM with Leray regularization for various N.

$$Nu = \frac{\int_{\Gamma_{top}} \nabla T \cdot \hat{n} dS}{\int_{\Gamma_{top}} dS}. \tag{39}$$

Fig. 10 shows the Nu history for the FOM and Galerkin ROM for different values of N. We observe that, even with the unconstrained Galerkin approach, the accuracy of the QOI can be recovered as the number of modes increases from $N = 10$ to 80. Fig. 11, however, illustrates that the stabilized Leray and constrained approaches are able to produce accurate Nu with much lower N (as low as 10) than the standard Galerkin approach.

5.2. 3D Rayleigh–Bénard convection

Three-dimensional thermal transients are of great importance to many thermal–hydraulic design questions and are thus of primary interest in our own ROM development efforts. Here, we test the ROM strategies on a 3D Rayleigh–Bénard problem in a box with aspect ratios $W : W : H$, where $W = 1$ and $H = 4$. The parameters are $Pr = 0.71$ and $Ra = 1.1e5, 1.1e6$ and $1.1e7$, which are implemented in (1)–(2) in convective time units by setting $\nu = (Pr/Ra)^{\frac{1}{2}}, \kappa = (PrRa)^{-\frac{1}{2}}$, and $\eta = 1$. The boundary conditions for velocity are no-slip on all walls. For temperature, the side-walls are insulated ($\nabla T \cdot \hat{\mathbf{n}} = 0$) and constant temperature on top and bottom, $T(x,y,z = \mp 2) = \pm 1$. Our FOM is based on the formulation in Nek5000 using an $8 \times 8 \times 32$ array ($x \times y \times z$) of 9th-order spectral elements. The FOM is based on 3rd-order semi-implicit timestepping with variable Δt set such that the Courant number is approximately 0.5 throughout the simulation, including the thermal transient.

Because this flow is three-dimensional and run at relatively high Rayleigh numbers the number of degrees-of-freedom is much greater than in the previous examples and these cases thus present a greater challenge for reduced-order modeling. Fig. 12 gives some indication of the number of active modes in the system in the fully-developed (statistically steady-state) regime as a function of Ra. On the left, we plot instantaneous temperature distributions from the FOM, and on the right we plot the fraction of energy, E_N/E captured by the POD bases from 1000 snapshots taken in the fully-developed flow regime. Here, $E_N = \sum_{j=1}^{N} (\zeta_j, \zeta_j)$, and $E := E_{1000}$.

From Fig. 12, right, we see that about 150 modes are required to capture 90% of the energy at $Ra = 1.1e7$. We have computed the critical Rayleigh number for this case (the point at which $\|\mathbf{u}\| > 0$) and find $Ra_c \approx 1559$, which makes the corresponding ratios for our three cases to be $r = Ra/Ra_c \approx 70, 700$, and 7000. Sirovich and Deane (1991) find that $N \approx 200$ modes are required for $E_N/E = 90\%$ when $r = 30$, which is a significantly more pessimistic outcome than our findings. Their case, however, corresponded to a unit-cube domain with periodic boundary conditions, which would support more degrees of freedom than our relatively narrow domain with walls. More recently, Puragliesi and Leriche (2012) examined the spectrum for $Ra = 10^9$ in a unit cube with

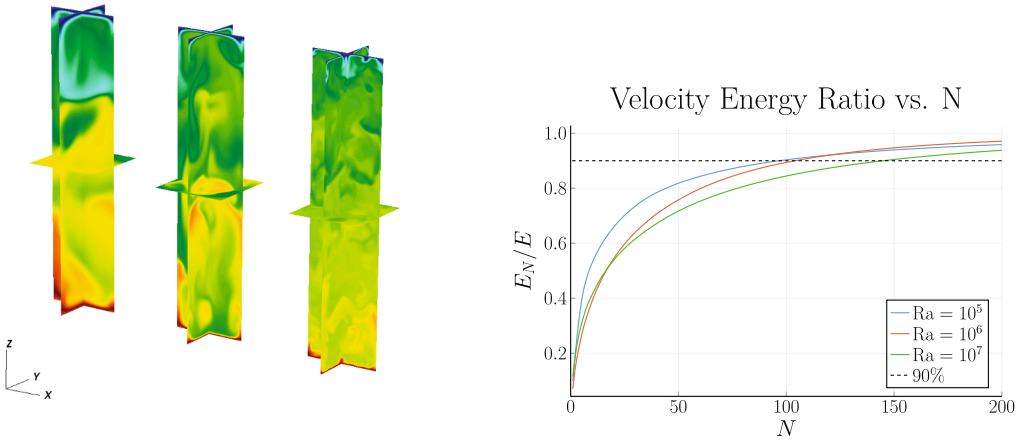

Fig. 12. Cross section at $x = 0, y = 0$ and $z = 0$ for FOM temperature at time $t = 1292$ with $Ra = 1.1e5, 1.1e6$ and $1.1e7$. Cumulative energy contribution of velocity POD modes for various Rayleigh numbers. The dotted line represents $E_N/E = 0.9$ where $E_N = \sum_{j=1}^{N} \lambda_j^2$ and $E = \sum_{j=1}^{K} \lambda_j^2$ where K is the number of snapshots and λ_i are the i-th eigenvalue of the Gramian.

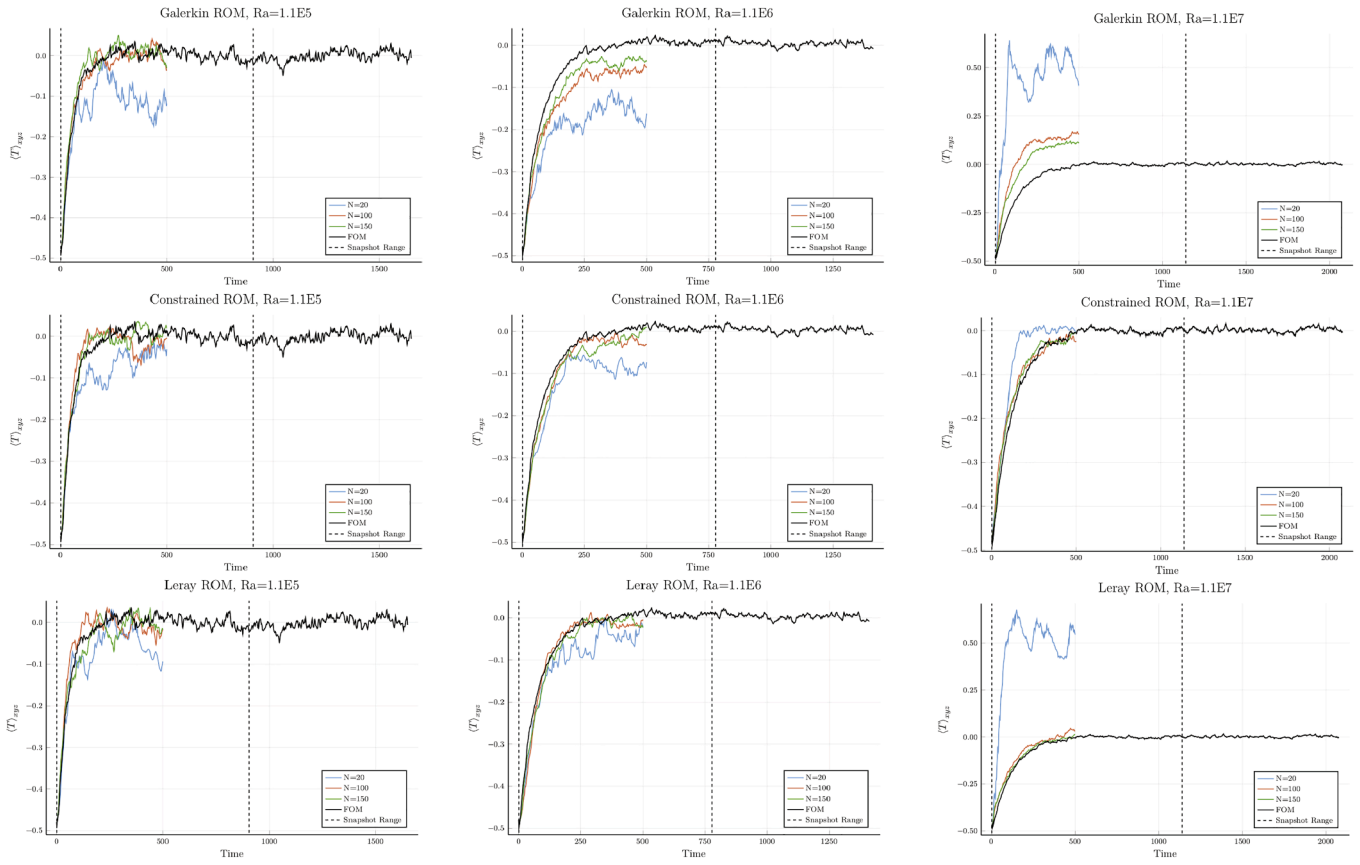

Fig. 13. 3D Rayleigh–Bénard convection: Average temperature vs. time with $Ra = 1.1e5, 1.1e6$ and $1.1e7$ for Galerkin, constrained ROM, and Leray ROM with various N. 70% of modes are filtered out in Leray ROM.1000 snapshots are taken between the two vertical dotted lines which includes the transient and statistically steady state region.

homogeneous Dirichlet conditions on all walls for the case where the side walls were differentially heated ($T\left(x = \pm\frac{1}{2}, y, z\right) = \pm\frac{1}{2}$.). In this case, they found that $N = 30$ sufficed to capture 90% of the energy. More importantly, Puragliesi and Leriche noted that the basis vectors that account for the majority of the heat flux are not the most energetic POD eigenfunctions, which implies that there is potential for a more judicious choice of basis functions when pMOR is employed for thermal transport problems.

In the present case, we are particularly interested in using the ROM (and, ultimately, pMOR) to capture thermal transients as rise time is of great interest in many thermal–hydraulics applications. To this end, we take as our QOI the mean temperature

$$\left\langle T \right\rangle(t)_{xyz} := \frac{\int_\Omega T(\mathbf{x}, t)\, dV}{\int_\Omega dV}. \tag{40}$$

The FOM starts with random fluctuations across all ($\mathcal{N} \approx 1.5$M) grid-points, uniformly distributed on $[-1, 0]$. This "cold" flow is then subject to boundary conditions ± 1 at time $t = 0+$, such that the mean should rise to $\langle T\rangle(t)_{xyz} \approx 0$. For the ROM, we take as the base state the first of the snapshots, which occurs at time $t \approx 1$.

Fig. 13 shows the transient behavior of $\langle T\rangle(t)_{xyz}$ for the Galerkin, constrained, and Leray ROMs at each of the three Rayleigh numbers. For Leray, we have tried filtering 10%, 30%, 50% and 70% of the modes report the results for the 70% case. Note that for different Ra, the optimal percentage to be filtered is different. For $Ra = 1.1e5$, all three formulations do a reasonable job of tracking the rise times for $N \geqslant 100$ modes. For $N = 20$, the Galerkin and constrained ROM do not do well while, surprisingly, the Leray ROM is able to produce a mean temperature that is comparable to constrained ROM. Furthermore, with 50% filtering (not shown), the Leray ROM with $N = 20$ is able to produce a even better mean temperature and is comparable to $N \geqslant 100$ modes. For $Ra = 1.1e6$, only the constrained and Leray ROM are able to track the QOI for $N = 100$ and 150. Moreover, the Leray ROM with 50% and 70% of modes filtered are able to track the QOI for $N = 20$. For $Ra = 1.1e7$, the Leray ROM is not stable for $N = 20$ with 70% of modes filtered (nor with 10%, 30% or 50%). While not terribly accurate in predicting the rise time, the constrained ROM is the only case that is stable for $N = 20$. Both the constrained and Leray approaches are accurate for $N \geqslant 100$.

In Fig. 14, left, we compare $\langle T\rangle$ for $Ra = 1.1e7$ with 1000 snapshots taken in the statistically steady-state region, using the average of the snapshots as the base mode. As the figure shows, without constraints, the mean temperature has more oscillations due to the lack of dissipation. For $N = 20$, the constrained and Leray ROMs produce a better QOI than the Galerkin ROM with $N = 100$. We also plot in the column on the right of Fig. 14 the turbulent kinetic energy (TKE) without zeroth mode, which we denote as $E_J := \frac{1}{2}\sum_{j=1}^{N} u_j^2$. We can see clearly that, even with $N = 100$, the Galerkin ROM drastically over-predicts the TKE. Note that we also observe over-prediction of TKE in the Leray ROM. In this case, even the constrained case shows an over-prediction of the TKE by about a factor of 2–3, which indicates that more modes are likely needed to capture this particular QOI. The fact that the thermal QOIs of Fig. 13 are in good agreement with the FOM is supportive of the suggestions of Puragliesi and Leriche (2012) that TKE is not necessarily directly correlated with the modes governing thermal transport.

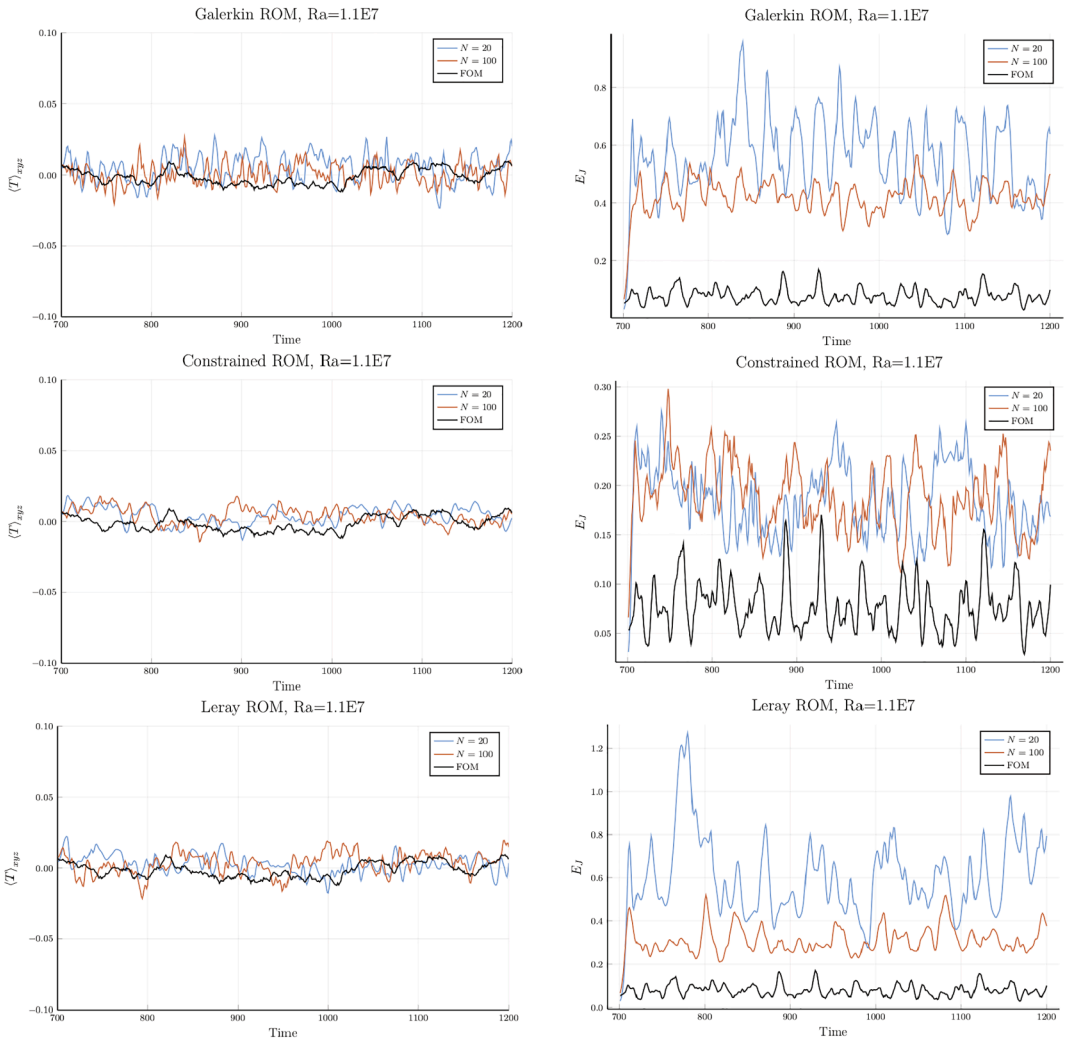

Fig. 14. 3D Rayleigh–Bénard convection; Left: Average temperature vs. time with $Ra = 1.1e7$ for Galerkin, constrained ROM, and Leray ROM with various N. Right: Turbulent kinetic energy (TKE) without zeroth mode vs. time with $Ra = 1.1e7$ for Galerkin, constrained ROM, Leray ROM with various N. 70% of modes are filtered out in Leray ROM.

6. ROM-FOM modeling for heat transfer

A common situation in thermal–hydraulics problems is to have widely disparate hydro and thermal time scales. This is often the case, for example, for forced convection in long ducts, pipes, or rod bundles, where the time for the turbulence to reach (statistically) steady-state conditions scales as a function of the hydraulic diameter, D_h, but the thermal transit time scales as the domain length, $L \gg D_h$. This situation is exacerbated in the case of conjugate heat transfer where the solid has thermal relaxation times $\gg$ the eddy turn-over times. In these cases, LES expends significant computational effort computing turbulent structures that have well-established (but not well known) statistics. Merzari et al. (2017) propose to resolve this scale disparity by using the full SEM basis representation to solve the transient thermal transport problem with a surrogate turbulent advector generated by a ROM for the hydrodynamics (which, crucially, avoids having to compute the pressure).

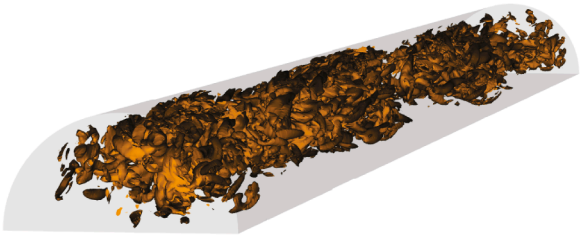

Fig. 15. Lambda 2 isocontour for Half-Pipe Flow at Re = 5,300.

To test this ROM-FOM idea, we consider 3D turbulent heat-transfer problem in a half-pipe of length $L = 15D_h$ with hydraulic diameter $D_h = 4A/P = 1$, where A is the half-pipe cross-sectional area and P is its perimeter. The parameters are $Re = 5300$ and $Pr = 5.858$. (In (1)–(2): $\nu = 1/Re, \kappa = 1/(PrRe)$, and $\eta = 0$.) The boundary conditions are periodic in the streamwise direction with heated side walls having uniform flux, $q'' = 1$. The forcing term is adjusted in time to ensure unit mean-velocity at each timestep. For the thermal problem, we write

$$T(x, y, z, t) = \theta(x, y, z, t) + \gamma z, \tag{41}$$

where θ is L-periodic, $\theta(x, y, z, t) \equiv \theta(x, y, z + L, t)$. Here, $\gamma = q'P$ is the mean streamwise thermal gradient and is determined by conservation of energy.

To develop the (hydro-only) ROM, the hydro FOM was run until the initial transient. 1000 snapshots were then collected over 1000 convective time units in the statistically stationary flow. The snapshots were used to produce $N = 200$ POD modes, which were used as the bases for the Galerkin hydro ROM with and without constraints. The resultant velocity fields were used to solve the forced convection problem in the

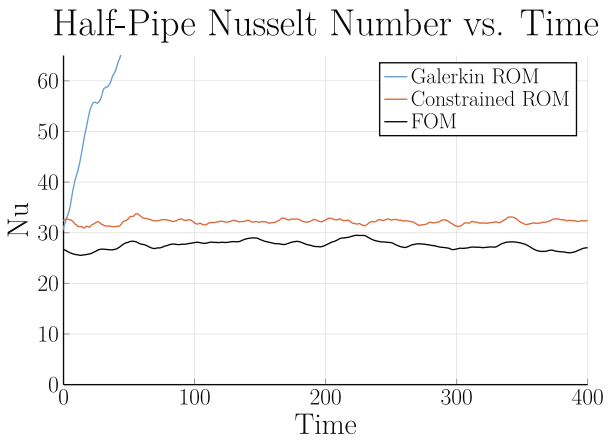

Fig. 16. Nusselt Number Comparison between Constrained ROM and FOM for Re = 5,300, Pr = 5.858.

half pipe and the Nusselt numbers were compared to those for the hydro-thermal FOM. Fig. 15 shows λ_2 (Jeong and Hussain, 1995) isocontours for a single snapshot, which gives insight into the number of structures present in this flow at $Re = 5300$.

In Fig. 16, we plot $Nu = (T_w - T_b)^{-1}$, where T_w is the average wall temperature and $T_b = \int wTdV / \int wdV$is the bulk temperature based on the streamwise velocity, w. For this modest (but turbulent) Reynolds-number case, the Galerkin ROM with $N = 200$ modes exhibits rapid departure from the FOM-based results for Nu. On the other hand, the constrained ROM provides a reasonably close estimate of Nu, with about 10% over-prediction.

Although we have not done so, one could also consider using just the off-line, full-ROM, model for prediction of Nu in this case as we did in our earlier 2D examples. Our objective here, however, is to establish the feasibility of using ROM-FOM to break the time-scale disparity for thermal–hydraulics problems in which snapshots for the full-order model are never available for the temperature.

7. Conclusions and future directions

We have presented several technical components towards the development of a reduced-order modeling (ROM) capability that aims to harness the output of high-fidelity simulations on leadership computing facilities for thermal–hydraulic design studies.

For the *parametric problem*, we have presented results for a p-greedy model-order reduction procedure applied to the problem of buoyancy-driven flows. We have demonstrated that the technique is capable of accurately predicting a challenging QOI—the period of roll-reversal—as a function of Rayleigh number for the highly nonlinear problem of Rayleigh–Bénard convection in a low aspect-ratio cylindrical domain.

At higher Rayleigh (and/or Reynolds) numbers, stabilization is required for POD-based ROMs. We have demonstrated that both Leray and constraint-based regularization generate more stable and more accurate solutions than the standard Galerkin-ROM formulation. Examples demonstrated that the constraint-based approach, which incorporates prior information about the long-time attractor in the ROM, can produce accurate transient solutions in 3D Rayleigh-Bénard convection at $Ra = 1.1e7$ and in forced convection in a half-pipe $Re = 5300$.

Despite the success of the methods shown here, several developments remain to make pMOR viable for engineering design. The first of these is a need to incorporate more (or better) modal information. Presently, the $O(N^3)$ costs in the ROM reconstruction phase prohibit consideration of N much larger than 200. There are several possible mitigation strategies. One idea is the discrete empirical interpolation method (Chaturantabut and Sorensen, 2010), which leads to low-rank approximations of the advection operator. For example, one can split the velocity as $\mathbf{u} = \mathbf{U} + \mathbf{u}'$ and then account for $\mathbf{U}\cdot\nabla\mathbf{U}, \mathbf{U}\cdot\nabla\mathbf{u}$, and $\mathbf{u}\cdot\nabla\mathbf{U}$, but neglect the $\mathbf{u}\cdot\nabla\mathbf{u}$ term (again giving rise to the classic turbulence closure problem). In our discrete model, this separation would lead to modeling the convective term by a interpolation function on the velocity coefficients in Eq. (11). (In some sense, sharp-cut-off Leray regularization is an example of this approach.) Another approach is to develop ROM and pMOR strategies that are optimized for the quantities of interest.

As indicated in the introduction, error indicators are of paramount importance for efficient pMOR design tools as they allow one to optimally select anchor points. We have initiated development of error indicators following the approach described in Fick et al. (2018). From the results of Section 5, it seems clear that error indicators that focus on the QOIs will be important for overall efficiency. Another concern is that the p-greedy pMOR strategy leads to an increase in N. In Fick et al. (2018), an h-greedy strategy is proposed in which one *changes* the approximation space, rather than *augmenting* the space, as the parameter p moves through the range of anchor space, $\mathscr{P}_\alpha$.

CRediT authorship contribution statement

Kento Kaneko: Writing - original draft, Writing - review & editing. **Ping-Hsuan Tsai:** Writing - original draft, Writing - review & editing. **Paul Fischer:** Supervision, Writing - review & editing.

Declaration of Competing Interest

The authors declare that they have no known competing financial interests or personal relationships that could have appeared to influence the work reported in this paper.

Acknowledgments

This research is supported by the DOE Office of Nuclear Energy under the Nuclear Energy University Program (Proj. No. DE_NE0008780). Simulations were performed at the DOE Office of Science User Facility ALCF (Argonne Leadership Computing Facility).

References

Barkley, D., Tuckerman, L.S., 1989. Traveling waves in axisymmetric convection: the role of sidewall conductivity. Physica D: Nonlinear Phenomena 37 (1–3), 288–294.
Chaturantabut, S., Sorensen, D.C., 2010. Nonlinear model reduction via discrete empirical interpolation. Journal of Scientific Computing 32 (5), 2737–2764.
Fick, L., Maday, Y., Patera, A.T., Taddei, T., 2018. A stabilized POD model for turbulent flows over a range of Reynolds numbers: Optimal parameter sampling and constrained projection. Journal of Computational Physics 371, 214–243.
Fischer, P., Kruse, J., Mullen, J. Tufo, H., Lottes, J., Kerkemeier, S., 2008. Nek5000: Open source spectral element CFD solver, Argonne National Laboratory, Mathematics and Computer Science Division, Argonne, IL, see https://nek5000.mcs.anl.gov.
Fischer, P., Schmitt, M., Tomboulides, A., 2017. Recent developments in spectral element simulations of moving-domain problems. Fields Institute Communications, Springer 79, 213–244.
Guermond, J.-L., Prudhomme, S., Oden, J.T., 2003. An interpretation of the Navier-Stokes-alpha model as a frame-indifferent Leray regularization. Physica D 177, 23–30.
Iollo, A., Lanteri, S., Désidéri, J.-A., 2000. Stability properties of POD–Galerkin approximations for the compressible Navier-Stokes equations. Theoretical and Computational Fluid Dynamics 13 (6), 377–396.
Jeong, J., Hussain, F., 1995. On the identification of a vortex. Journal of Fluid Mechanics 285, 69–94.
Khodkar, M., Hassanzadeh, P., Nabi, S., Grover, P., 2019. Reduced-order modeling of fully turbulent buoyancy-driven flows using the Green's function method. Physical Review Fluids 4, 1, 013801.
Lui, H.F.S., Wolf, W.R., 2019. Construction of reduced-order models for fluid flows using deep feedforward neural networks. JFM 872, 963–994.
Merzari, E., Ninokata, H., Mahmood, A., Rohde, M., 2009. Proper orthogonal decomposition of the flow in geometries containing a narrow gap. Theoretical an Computational Fluid Dynamics 23 (5), 333–351.
Merzari, E., Pointer, W.D., Fischer, P., 2011. A POD-based solver for the advection-diffusion equation. In: ASME-JSME-KSME 2011 Joint Fluids Engineering Conference. American Society of Mechanical Engineers Digital Collection, pp. 1139–1147.

Merzari, E., Obabko, A., Fischer, P., Halford, N., Walker, J., Siegel, A., Yu, Y., 2017. Large-scale large eddy simulation of nuclear reactor flows: Issues and perspectives. Nuclear Engineering and Design 312, 86–98.

Mullen, J., 1999. Development of a Parallel Spectral Element Based Large Eddy Simulation Model for the Flow of Incompressible Fluids in Complex Geometries, Ph. D. thesis, Brown University, division of Engineering.

Nocedal, J., 1980. Updating quasi-Newton matrices with limited storage. Mathematics of Computation 35 (151), 773–782.

Orszag, S., Israeli, M., Deville, M., 1986. Boundary conditions for incompressible flows. Journal of Scientific Computing 1, 75–111.

Puragliesi, R., Leriche, E., 2012. Proper orthogonal decomposition of a fully confined cubical differentially heated cavity flow at Rayleigh number Ra = 109. Computers & Fluids 61, 14–20.

Rempfer, D., 2000. On low-dimensional Galerkin models for fluid flow. Theoretical and Computational Fluid Dynamics 14 (2), 75–88.

Sirovich, L., Deane, A.E., 1991. A computational study of Rayleigh–Bénard convection. Part 2. Dimension considerations. Journal of Fluid Mechanics 222, 251–265.

Tomboulides, A., Israeli, M., Karniadakis, G., 1989. Efficient removal of boundary-divergence errors in time-splitting methods. Journal of Scientific Computing 4, 291–308.

Tomboulides, A., Lee, J., Orszag, S., June 1997. Numerical simulation of low mach number reactive flows. Journal of Scientific Computing 12, 139–167.

Wells, D., Wang, Z., Xie, X., Iliescu, T., 2017. An evolve-then-filter regularized reduced order model for convection-dominated flows. International Journal for Numerical Methods in Fluids 84 (10), 598–615.